Ocean Engineering 270 (2023) 113443

Contents lists available at ScienceDirect

Ocean Engineering

journal homepage: www.elsevier.com/locate/oceaneng

Marine propeller underwater radiated noise prediction with the FWH acoustic analogy Part 2: Assessment of model scale propeller hydroacoustic performance under non-uniform flow conditions

Savas Sezen [a,b,*], Mehmet Atlar [b]

[a] Lloyd's Register (LR) EMEA, UK
[b] Department of Naval Architecture Ocean, & Marine Engineering, University of Strathclyde, Glasgow, UK

ARTICLE INFO

Handling Editor: Prof. A.I. Incecik

Keywords:
AMR
DES
URN
The princess Royal
TVC

ABSTRACT

This study presents the model scale benchmark, The Princess Royal, propeller's hydrodynamic performance, including cavitation extensions and URN operating in a non-uniform wake field. The developed V-AMR technique was used in the numerical calculations to accurately solve the tip vortex flow and better representation the tip vortex cavitation (TVC) in the propeller slipstream. The sheet and tip vortex cavitation was modelled using the Schnerr-Sauer cavitation model. A hybrid method, combining the DES and permeable formulation of the FWH equation, was used for predicting the propeller URN at four different operating conditions corresponding to full-scale operating conditions. The numerical results were first validated with the experimental data obtained in the cavitation tunnel through the propeller hydrodynamic characteristics, cavitation extension and URN in model scale. Then, the propeller URN predictions using a hybrid method were extrapolated to full-scale with the ITTC extrapolation procedure to compare the numerical results with the extrapolated experimental data and full-scale measurements. The results showed that the cavitation extensions on and off the blades were satisfactorily predicted in the numerical calculations compared to the model-scale campaigns and full-scale sea trial observations. However, the same cavitation dynamics and TVC could not be predicted in conditions where the weak and incipient TVC were present between the numerical calculations and model-scale test campaign. Also, the numerical calculations underpredicted the model scale propeller URN at certain frequencies compared to model scale experimental data, except for the highest loading condition. Akin to the comparisons of model scale propeller URN between the numerical calculations and model-scale test data, the extrapolated propeller URN was generally underpredicted at a certain frequency range of the noise spectrum in the numerical calculations compared to the full-scale measurements. This underprediction in the numerical calculations can be associated with the lack of cavitation dynamics, especially TVC, compared to experimental and full-scale observations.

1. Introduction

The substantial growth of ship numbers and sizes causes a considerable increase in noise pollution in the world's oceans. Ship traffic is deemed the main noise source contributing to the ambient noise levels, particularly at low frequencies (Erbe et al., 2019). Thus, the concern for the potential environmental impacts of ship noise on marine animals has risen over the years. In this regard, several research studies have been carried out to investigate the influence of increased URN (Underwater Radiated Noise) levels on marine animals in the literature (Nowacek et al., 2007; Slabbekoorn et al., 2010). To address the increased URN levels due to commercial shipping, the International Maritime Organisation (IMO) recognised this issue and published a non-mandatory guideline to mitigate the URN levels radiated by commercial ships to decrease the short and long term negative impacts on marine life (IMO, 2014). This guideline identified several alternative ways to reduce the URN levels for retrofit and new built commercial vessels. Also, it was stated that there are still some research and knowledge gaps in identifying the contribution of different sources on URN levels. The steady increase in URN levels in the oceans has further escalated interest in this field. Recently, the Marine Environment Protection Committee of the IMO has accepted the proposal from Australia, Canada and the United States to review the existing 2014 Guidelines to reduce underwater noise from commercial shipping (Breeze et al.,

* Corresponding author. Lloyd's Register (LR) EMEA, UK.
E-mail address: savas.sezen@lr.org (S. Sezen).

https://doi.org/10.1016/j.oceaneng.2022.113443
Received 28 May 2022; Received in revised form 19 September 2022; Accepted 13 December 2022
Available online 5 January 2023

2022).

The main hydroacoustic noise source radiating from a commercial ship is the cavitating propeller, even if the hydrodynamic flow noise and machinery noise can significantly contribute to the overall noise levels at certain operating conditions. However, when the cavitation occurs on and off the blades, the cavitating propeller will dominate all relevant noise sources radiated by the ships. The avoidance and delay of the cavitation on marine propellers can be possible for warships and submarines. Hence, considerable effort is given at the design stage to increase the cavitation inception speed (CIS) to avoid cavitation. On the other hand, the complete elimination of the cavitation is not possible for the commercial vessel's propeller to meet the required speed and power criteria. Although there are advanced techniques for mitigating cavitation (e.g., active and passive control methods) and hence cavitating propeller URN, these techniques may not provide a complete solution. They might be quite expensive to be implemented in the marine propellers. Besides, they may also reduce efficiency, increasing fuel consumption and greenhouse gas emissions (Leaper et al., 2014).

Cavitation is a complex flow phenomenon and influences the hydrodynamic and hydroacoustic performance of the propeller considerably. The cavitation dynamics considerably affect the broadband noise characteristics and discrete peaks at the blade passage frequencies. The growth and collapse of individual bubbles in the water create broadband noise, whereas the volume variation of the sheet and tip vortex cavitation generates discrete peaks (IMO, 2014; ITTC, 2017a). For this reason, the accurate prediction and modelling of the cavitation and hence associated cavitating propeller noise became an important research area in the hydrodynamic field. The current methods for the URN predictions mainly utilise the experiments conducted in the cavitation tunnels, which requires a well-established experimental setup to replicate the ship wake and the cavitation conditions as in the full-scale condition (Aktas et al., 2016b). Although the experimental and semi-empirical methods are still popular approaches for the propeller URN prediction, the capabilities of the CFD tools and understanding of the complex flow phenomena, particularly under cavitating conditions, are improving. Therefore, in the future, similar to other ship hydrodynamic problems, the CFD based methods will be expected to become the frontline for the propeller URN prediction and hence propeller design/optimisation studies (Stark and Shi, 2021). The CFD tools used for the propeller URN predictions both in near and far fields can be classified as follows:

- Direct Numerical Simulation (DNS) to solve all turbulent scales
- Direct viscous-based CFD methods (i.e., LES, DES and RANS)
- Viscous-based hybrid methods (i.e., hydrodynamic solver with the acoustic analogy)

DNS is computationally expensive, and it is not possible to perform such a hydroacoustic simulation with the current resources. The alternative CFD methods can be utilised to predict the hydroacoustic performance of a propeller. Amongst them, LES is a capable method of directly solving the large turbulence scales and modelling the small scales, whereas the RANS is based on the solution of time-averaged equations. DES is an alternative method, and it uses the advantages of LES and RANS methods. However, any direct solution requires governing equations based on compressibility assumption. This is because the sound is defined as a pressure fluctuation, and it propagates at a finite speed in a medium. Under the isentropic flow hypothesis, the speed of sound is defined by $(c_0^2 = dp/d\rho)$ and hence the incompressibility assumption $(d\rho = 0)$, used for propeller hydrodynamic performance prediction, makes the sound speed infinite $(c_0 = \infty)$. This results in ignoring the sound propagation from near to far-field. Due to this fact, any direct methods under the incompressibility assumption are not suitable for hydroacoustic predictions in the far-field. Besides, the implementation of the CFD methods under compressibility assumption for the propagation of the sound to the desired location is an expensive approach, especially for high Reynolds number flows, because the high-fidelity and high order methods are required to prevent dissipation or dispersion of the acoustic field. For this reason, in general, the source and propagation field is decoupled using hybrid methods (Nitzkorski, 2015). Once the source field is solved and the sound source is predicted using the high-fidelity CFD tools, the acoustic analogies are used to propagate sound from near to far-field (Ianniello et al., 2013). In other words, the acoustic analogy adds compressibility effects to the incompressible hydrodynamic solver and uses input values derived by the incompressible hydrodynamic solver to compute acoustic pressure (Sezen and Kinaci, 2019).

Amongst different integral based acoustic analogies, the Ffowcs Williams Hawkings (FWH) is the most popular and efficient formulation for aeroacoustics and hydroacoustic problems. In particular, to include the contribution of nonlinear noise sources mainly represented by turbulence and vortex structures, the porous/permeable formulation of FWH is generally utilised as the direct solution of the volume integrals (i.e., quadrupole noise terms/nonlinear noise source terms) are computationally expensive. The application of porous FWH formulation for hydroacoustic problems is rather new, and there is no standard practice yet. Despite this, there are several studies conducted using the porous FWH formulation using the different CFD methods for the investigation of propeller URN under non-cavitating and cavitating conditions (e.g., Ianniello et al., 2013; Ianniello and De Bernardis, 2015; Lloyd et al., 2015; Testa et al., 2018; Savas Sezen et al., 2020; Sezen et al., 2021a). It is worth mentioning that the research in this field was mainly conducted under uniform flow conditions to eliminate the influence of hull wake and shaft inclination for the validation and investigation purposes of the hybrid methods before the complex scenarios (e.g., in the presence of hull wake). However, in reality, the marine propellers are always operating behind the ship, hence in the presence of a non-uniform wake. The interaction between the wake of a ship and the propeller alters the blade loading, cavitation dynamics and hence associated pressure pulse and URN characteristics. Thus, the propeller URN prediction will be more important in the presence of a non-uniform wake than the predictions conducted under uniform flow conditions. In this regard, Bensow and Liefvendahl (2016) predicted the cavitating propeller URN in the presence of hull and shaft inclination using the LES together with the porous FWH equation. The numerical results, including cavitation patterns and propeller URN, were validated with the experimental data measured in the cavitation tunnel. The results showed good agreement with the experimental data after 1 kHz, whereas the numerical prediction underpredicted the noise levels in the low-frequency region. The differences between numerical prediction and experiment were mainly deemed to lack sheet and tip vortex cavitation dynamics predicted in the numerical calculations compared to the experiment. Hallander et al. (2012) investigated the propeller URN in the presence of hull wake for an LNG ship under non-cavitating and cavitating conditions. The unsteady RANS method with the FWH, two different potential based solvers and a semi-empirical formulation was used in the computations. The obtained results were validated with the experimental data. Although the results up to 200Hz showed good agreement with discrepancies using the RANS with FWH, it was stated that the limitations of the RANS approach caused the underprediction of the broadband part of the noise spectrum. Later on, the authors repeated the calculations using the advanced CFD method (i.e., DDES) and FWH acoustic analogy to predict propeller URN at the model and full-scale (Li et al., 2015). In their previous study, due to the capabilities of the RANS, the contribution of nonlinear noise sources originating from the instantaneous stress tensor and turbulent eddies could not be predicted accurately. However, with the application of the DDES method, this issue was rather solved, and the results showed better agreement with the experimental and sea trial data up to the mid-frequency region. Nevertheless, due to the insufficient modelling of TVC, the numerical results deviated compared to experimental data at a certain frequency range. Fujiyama and Nakashima (2017) explored the cavitating propeller URN using the hybrid

method for both model and full-scale ships. The cavitation patterns at different angles were compared with the experimental data. The sheet and tip vortex cavitation could be observed successfully in the numerical calculations in model scale, whereas the interaction between the sheet and TVC could not be captured in full-scale. The noise predictions were in good agreement with the experimental data up to 5^{th} BPF for model scale and 1^{st}-2^{nd} BPF for full-scale propeller, respectively. In the study of Lidtke et al. (2019), the hydrodynamic performance of the INSEAN E779A propeller was investigated under non-cavitating and cavitating conditions in the presence of non-uniform flow using the RANS with porous FWH formulation. In this study, the several noise modelling parameters (e.g., definition of the porous surface, influence of time step and grid resolution) were investigated. The pressure amplitude comparisons between the numerical results and experiments showed good agreement with the receivers located sides and above the propeller, whereas the pressures were overpredicted in the numerical calculations compared to experimental data for the receivers located downstream. It was also stated that the future work will focus on the further refinement for the modelling of tip vortex dynamics as the current method suffered from insufficient tip vortex modelling in the propeller slipstream.

Despite the few studies conducted in this research field for the investigation of cavitating propeller URN under non-uniform flow conditions (or behind hull conditions), at present, the numerical propeller URN predictions, which can be achieved using the CFD methods together with the FWH acoustic analogy, still need more validation and verification studies to show the capabilities of the CFD methods at several operating conditions, especially under non-uniform flow conditions. For this reason, this study aims to fill this research gap using the state of art CFD method together with the porous formulation of the FWH equation for the benchmark propeller (i.e., The Princess Royal). The authors also incorporated their recently developed advanced meshing technique (i.e., Vorticity-based Adaptive Mesh Refinement) with the noise modelling to accurately solve the tip vortex and better represent the TVC in the propeller slipstream and include its effects on propeller URN.

In this study, the cavitating flow around the benchmark propeller was solved using a high-fidelity DES method together with the k-ω SST turbulence model in the facilities of Star CCM+ (Star CCM+ 14.06, 2019). The sheet and tip vortex cavitation was modelled using the mass transfer model. To better realise the TVC in the propeller slipstream, the Vorticity-based Adaptive Mesh Refinement procedure (V-AMR) developed and proposed by the authors (Sezen and Atlar, 2021) was utilised. The non-uniform wakefield data, measured in the Ata Nutku Towing tank of Istanbul Technical University, was used for the numerical calculations. The hydrodynamic performance, including cavitation patterns, was first validated with the experimental and sea trial data at four different full-scale operating conditions. Then, the propeller URN predictions were also validated with the measurements conducted in the GENOA cavitation tunnel at different receiver locations for the model scale propeller. Consequently, the URN predictions were extrapolated to full-scale using the ITTC procedure and validated with the sea trial and extrapolated measured data. The numerical results were discussed, and the pros & cons of the adopted numerical approach were presented.

In our Part 1 study, the hydroacoustic performance of The Princess Royal propeller was predicted for the uniform flow conditions. In this study (i.e., Part 2), the numerical investigations were extended for the same benchmark propeller operating under a non-uniform flow field corresponding to the full-scale operating conditions. Following this, the numerical calculations were also carried out in full-scale in the presence of a hull, and the reliability of the presented approach was shown at the far-field where the sea trial data was collected during the sea trials in our Part 3 study.

The paper is organised as follows. Section 2 presents the theoretical background of the study. The numerical modelling is presented in Section 3, whereas the numerical results are given in Section 4. Consequently, the concluding remarks are given in Section 5.

2. Theoretical background

2.1. Hydrodynamic model

The numerical computations were carried out using the commercial CFD software, Star CCM+ 14.06 (Star CCM+ 14.06, 2019). In order to solve the flow around the cavitating marine propeller, the DES method was utilised as it is a hybrid method combining the RANS in the boundary layer and LES in the free flow region of the computational domain. Thus, this method is a good compromise for accurately capturing the flow details that RANS is not capable of without the high computational effort required by LES, particularly through near-wall modelling. Among the different variants of the DES method, DDES (Delayed Detached Eddy), the upgraded version of the standard DES method, was used together with the k-ω SST turbulence model to solve the interaction between the transient behaviour of the cavitation flow and turbulence and hence accurate propeller URN prediction. DDES method incorporates a delay factor that improves the model's ability to separate between LES and RANS regions. In this way, the RANS and LES regions inside the computational domain can be distinguished. In our case, the boundary layer solution was provided by the RANS method, whereas LES was used for the solution of flow details in the propeller slipstream (Star CCM+ 14.06, 2019 and Spalart et al., 1997).

The cavitation modelling is based on the homogenous two-phase flow assumptions. Within the facilities of the commercial solver (i.e., Star CCM+ 14.06, 2019), two different cavitation models are present, namely the full Rayleigh-Plesset model and the Schnerr Sauer model. The bubble growth rate is determined by solving the Rayleigh-Plesset equation in its complete form in the full Rayleigh Plesset model. In contrast, the bubble growth rate is determined using a simplified expression in the Schnerr Sauer cavitation model. Although the dynamic cavitation process where the effects of bubble inertia, viscous diffusion, etc., are important is modelled more accurate in the full Rayleigh-Plesset model than the Schnerr Sauer cavitation model, the full Rayleigh-Plesset model requires smaller time steps, resulting in an increased computational cost of the solution. Thus, the Schnerr-Sauer cavitation model, which has been used in several studies in the literature, was used in this study. Besides, the accuracy of the Schnerr Sauer cavitation model has been shown in different engineering problems in the literature. (Schnerr and Sauer, 2001; Muzaferija et al., 2017; Star CCM+ 14.06, 2019).

2.2. Hydroacoustic model

The DDES method was used to assess flow field solution in the near field and provided the required hydrodynamic inputs to the acoustic analogy. FWH (Ffowcs Williams and Hawkings, 1969) acoustic analogy was used for noise propagation. This acoustic analogy rearranges the governing equations into the inhomogeneous wave equation. Here, the different noise generation mechanisms are defined, and these noise generation mechanisms are expressed by different source terms. Amongst the different integral based acoustic analogies, the permeable FWH equation was used in this study to include the contribution of nonlinear noise sources (e.g., turbulence and vorticity), including TVC, within the permeable surface. The reason is that the DES method was used to accurately solve the turbulent and vorticity structures in the propeller slipstream and the interaction between the turbulence and cavitation dynamics. Thus, the contribution of this resolved turbulence and vorticity structures occurring in the propeller slipstream on overall acoustic pressure can be significant even if the propeller is operating under cavitating conditions. This contribution can be included effectively using the permeable FWH formulation.

The permeable FWH formulation, which was first implemented and proposed by Ffowcs Williams and Hawkings (1969) and proposed as a possible numerical solution of the FWH equation by Di Francescantonio (1997) requires a fictitious integral surface, which encompasses the propeller and the relevant portion of the propeller slipstream to account

for the contribution nonlinear noise sources. The permeable FWH formulation can be derived by introducing modified velocity (U) and stress tensor (L) using the generalised formulation of the FWH equation, and it can be written as follows (Farassat, 2007);

$$\Box^2 p = \frac{\partial}{\partial t}\left[\rho_0 U_n \delta(f)\right] - \frac{\partial}{\partial x_i}\left[L_{ij} n_j \delta(f)\right] + \frac{\partial^2 T_{ij}}{\partial x_i \partial x_j} \quad (1)$$

Here, $\Box$ is the wave or D'Alembertian operator in three-dimensional space, n is unit outward normal, ρ_0 is the speed of density in the undisturbed medium, p is the acoustic pressure, T_{ij} is the Lighthill stress tensor. $\delta(f)$ and are the Dirac delta function. In this equation, the first term represents the pseudo-thickness, while the second is the pseudo-loading noise term. The last term is the quadrupole (or nonlinear noise) term outside the integral surface. The permeable FWH formulation enables the evaluation of the nonlinear noise sources encapsulated by the integral surface using the surface integral. This makes the formulation very appealing because the solution of volume integral in the general form of FWH formulation is computationally expensive and it requires high computational memory. When the permeable FWH formulation is applied, the vortices passing through the downstream end of the permeable surface can create spurious noise due to truncation errors of the source terms at the permeable surface boundary. Thus, this spurious noise can contaminate the overall acoustic prediction. This is also known as the end-cap problem in literature (Nitzkorski, 2015; Wang et al., 2018). The end-cap problem is associated with the differences between acoustic and hydrodynamic pressure distributions described in Ffowcs Williams, 1992 (Testa et al., 2021). In order to remove such spurious noise, ad hoc techniques are implemented to remove the artificial boundary noise (e.g., Wang et al., 1996; Ikeda et al., 2017). To decrease the spurious noise issue, the permeable surface can be located far from the flow region where the vorticity is still present. However, this leads to the risk of information loss because of the numerical dissipation and discretisation errors. Even if one attempts to adopt fine grid resolution for the entire large permeable surface to minimise the numerical dissipation, this will inevitably increase the computational cost of the solution and is not practical. Alternatively, the complete FWH equation, including the volume integral terms outside of the integral surface, can be solved to complete elimination of this issue. However, this will also increase the computational cost of the solution considerably. Therefore, in our study, the contribution of quadrupole noise sources outside of the permeable surface was neglected. Also, a relatively small permeable surface, which included of the most energetic part of the vortex structures in the propeller slipstream, was used based on our understanding the flow details in the propeller slipstream. The permeable surface was extended 0.6*D upstream and 1.4*D downstream from the propeller blades' centre (i.e., total length 2*D) with a diameter of 1.25*D. Therefore, the investigation of the end-cap problem was left out of the scope of this paper.

3. Test case setup and numerical modelling

3.1. Propeller geometry and test matrix

The five-bladed benchmark propeller, Princess Royal, was used in the numerical calculations (Atlar et al., 2013). This propeller has been used for the cavitation observation and propeller URN predictions in the scope of the ongoing round-robin (RR) test campaign to compare the results and understand the possible differences obtained by different facilities (Tani et al., 2020). The model propeller's main particulars and 3D view are given in Table 1 and Fig. 1, respectively.

The propeller operating conditions were defined according to torque and cavitation number identity during the measurements at the University of Genoa (UNIGE) cavitation tunnel to reproduce the full-scale operating conditions in model scale (Aktas et al., 2016a; Tani et al., 2019). The experimental setup and tests details can be found in the study

Table 1
The main particulars of the propeller.

Parameters	Model Scale Princess Royal Propeller
Diameter, D (m)	0.22
P/D at 0.7R	0.8475
Expanded Blade Area Ratio	1.057
Blade Number, Z	5
Rake (°)	0
Skew (°)	19

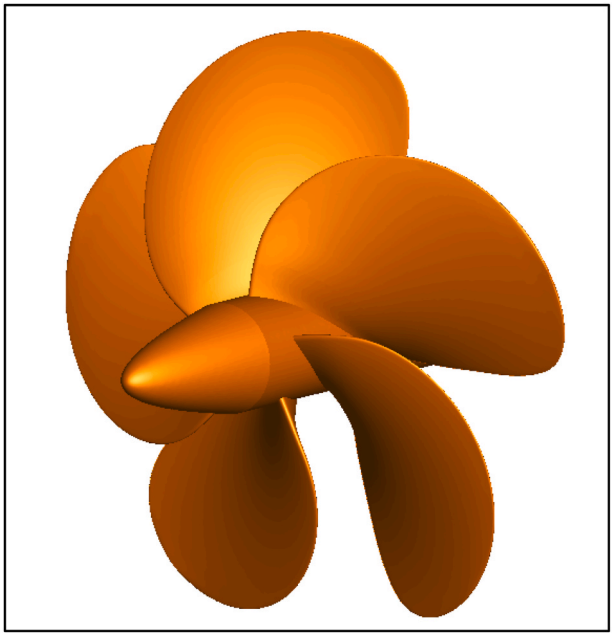

Fig. 1. 3D view of the benchmark Princess Royal propeller.

Tani et al. (2019). The operating conditions investigated in this study are summarised in Table 2.

The cavitation number is calculated based on the propeller rotational rate as follows;

$$\sigma_N = \frac{P_0 - P_V}{0.5\rho(nD)^2} \quad (2)$$

Here, n is the propeller rotation rate, P_0 is the static pressure, P_V is the vapour pressure, and ρ is the water density.

During the experiment, a wire screen was built iteratively to measure the resulting flow field using a 2D-LDV device until a similar non-uniform wake field was found compared to the target wake field measured at Ata Nutku towing tank at Istanbul Technical University (Korkut and Takinaci, 2013). As shown in Fig. 2, the resulting wake field is compared with the target wake field. As stated in the study of Tani et al. (2019), the reason for missing values on the left side of the polar graph was the LDV beams' accessibility in the tunnel. The target wake field measured at the towing tank was used in the numerical calculations

Table 2
Test matrix.

Test Condition	FULL-SCALE				MODEL-SCALE	
	Engine RPM	Shaft RPM	Shaft rate (RPS)	STW (knot)	n (rps)	$\sigma_N(nD)$
C1	900	514	8.6	7.1	25	5.28
C2	1200	682	11.4	9.4	35	3.00
C3	1500	856	14.3	10.5	35	1.91
C4	2000	1141	19.0	15.1	35	1.07

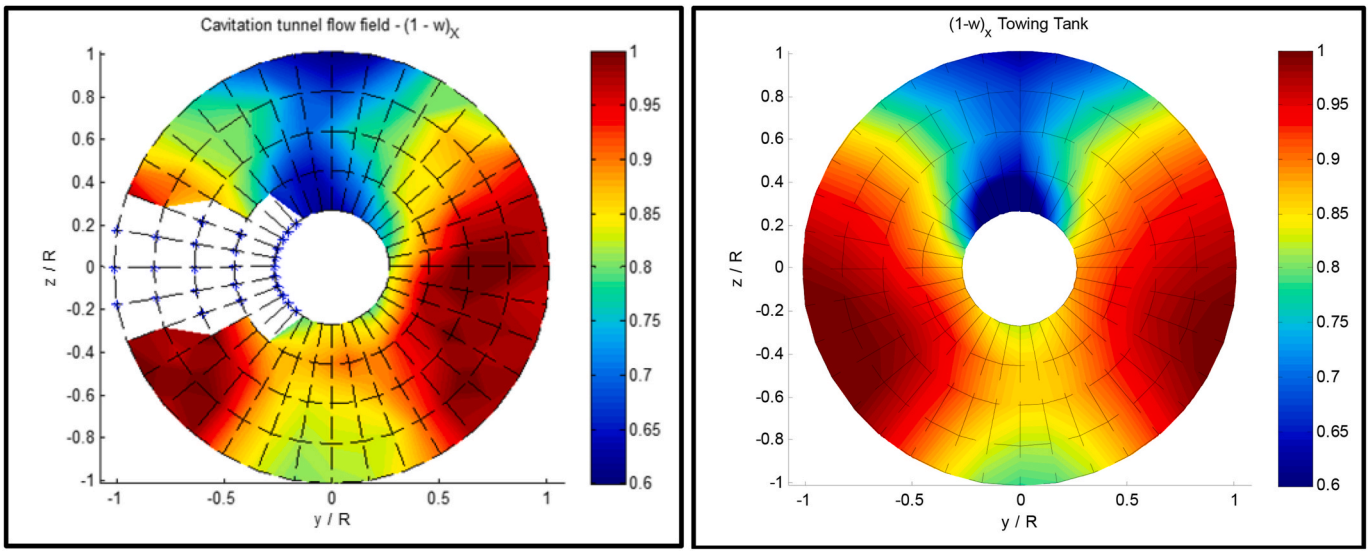

Fig. 2. Nominal wakefield at the propeller plane (Left: simulated wakefield in the cavitation tunnel, right: target wakefield measured in the towing tank) (Tani et al., 2019).

with three velocity components (i.e., axial, tangential and radial) at different operating conditions.

3.2. Numerical modelling

3.2.1. Computational domain and boundary conditions

The GENOA cavitation tunnel measurement section was replicated in the numerical calculations and hence dimensions of the computational domain were set to 2.2m total length, 0.57m height, and 0.57m width from the centre of the propeller blades. Fig. 3 shows the computational domain and boundary conditions defined in the numerical calculations. The positive X direction was identified as velocity inlet, whereas the negative X direction was defined as pressure outlet. The target wake field was imposed on the inlet to operate the propeller under non-uniform flow conditions. The remaining surfaces of the domain, propeller, shaft, and hub were defined as no-slip walls. There are three regions within the computational domain: static, rotating, and noise regions. Internal interfaces were created to connect these regions. The propeller rotational motion was provided using the rotating region, whereas the outer cylinder surface (i.e., noise region) was used for propeller URN predictions.

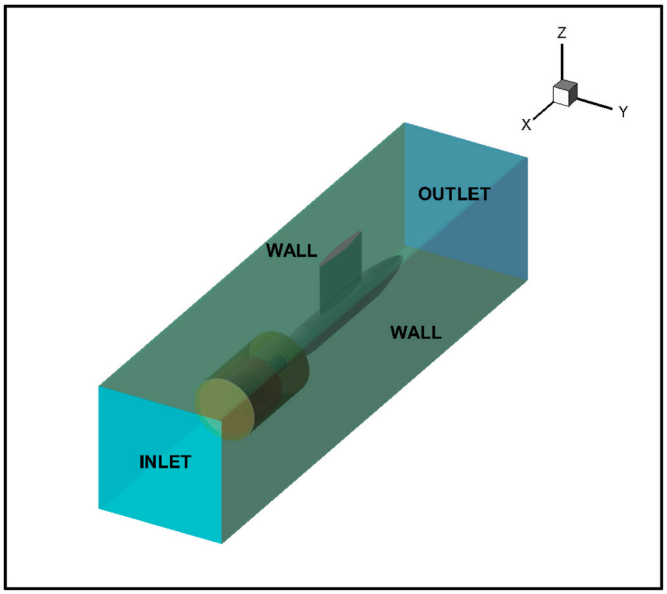

Fig. 3. Representation of computational domain used in the numerical calculations.

3.2.2. Grid generation

The accuracy of the numerical solution can be affected by several parameters (e.g., numerical scheme, timestep selection, turbulence modelling, etc.). Amongst them, the grid quality is the most important one influencing the representation of the complex geometry, the accuracy of the solution and its convergence. The tip vortex cavitation (TVC), which is the first type of cavitation occurring on a well-designed propeller and one of the important noise sources, modelling has always been a challenge. The reason is that anisotropic turbulence and high-velocity gradients in all directions inside the vortex core make the assessment of tip vortex flow are difficult (Asnaghi et al., 2020). In general, the local mesh refinements (e.g., spiral and tube) have been implemented using fine grid resolution in the propeller slipstream to decrease the numerical diffusion at the tip region. Alternatively, one can adapt the fine grid resolution entire propeller slipstream to solve the flow inside the tip vortex accurately. However, these approaches are computationally expensive unless sophisticated methods are used with proper numerical set-up for model and full-scale marine propeller applications.

In this regard, the authors have recently introduced the Vorticity-based Adaptive Mesh Refinement (V-AMR) technique for the accurate solution of the tip vortex flow and hence tip vortex cavitation (TVC) observation in the propeller slipstream (Sezen and Atlar, 2021). Using the V-AMR technique, the grid is refined as local as possible in the vicinity of tip vortex areas to reduce the computational cost of the solution. This technique consists of two stages, namely 1st stage V-AMR and 2nd stage V-AMR and two stages V-AMR procedure enables to reduce the computational cost of the solution. In the 1st stage, the relatively coarse grid reveals the tip vortex trajectory in the propeller slipstream. Following this, 2nd stage V-AMR is implemented using the fine grid resolution. The authors have shown the feasibility and accuracy of this technique with different benchmark propellers using different numerical methods (e.g., RANS, DES and LES). Therefore, in this study, the same V-AMR technique was implemented for the observation of TVC under non-uniform flow conditions. Detailed information about the application of this technique can be found in the study of Sezen and Atlar (2021).

The grid quality is also crucial for accurately predicting propeller URN. The low-quality cells cause deterioration of the solution accuracy, divergence, numerical and spurious noise. Therefore, the adapted mesh should be able to resolve the turbulence scales and propagate the sound from near to the far-field. In a recent study conducted by the authors (Sezen et al., 2021b), the influence of grid resolution on propeller hydroacoustic performance was comprehensively investigated and it was shown that the hydroacoustic performance prediction of the propeller was more dependent on grid resolution compared to the prediction of global performance characteristics such as thrust, torque and efficiency. Thus, in this study, based on our recent investigation, the uniform grid resolution in all directions and smooth mesh transitions were applied as much as possible. The abrupt mesh changes were avoided at the transition regions to minimise the possible spurious sound waves at the interfaces, which can pollute the results. In the numerical calculations, trimmed cells (unstructured hex-meshes) were used as they provide the least amount of dissipation for finite volume schemes and are less dissipative than polyhedral meshes. The grid was refined in all directions to achieve the $y^+ < 1$ to resolve the boundary layer itself to increase the accuracy of the solution. In order to solve the tip vortex accurately and observe the TVC, the V-AMR technique was also implemented using the mesh table based on user-based field functions obtained for each operating condition. The total element count was calculated at around 24M. The grid structure used in the numerical calculations can be seen in Fig. 4.

3.2.3. Analysis properties

The application of the DES method can be challenging unless suitable simulation properties are selected. In the numerical calculations, a segregated flow solver and a SIMPLE algorithm were used to compute the velocity and pressure. The Hybrid Bounded Central Differencing Scheme (Hybrid-BCD) was used for the segregated solver to discretise convection terms in the momentum equations. This scheme blends second-order upwind and bounded central differencing, and the blending factor is calculated according to the flow field features. This discretisation scheme is also advisable for DES methods. Furthermore, the second-order discretisation scheme was also utilised for the convection of turbulence terms (Star CCM+ 14.06, 2019).

The second-order implicit numerical scheme was used for the time discretisation. For the DES method, the time step selection is also an important parameter linked to the CFL number inside the domain. In this regard, the timestep was selected as 0.5° of the propeller rotational rate (i.e., 3.96×10^5) at different operating conditions. As the implicit scheme was utilised, the CFL number is not associated with the stability of the time scheme, but keeping the CFL around 1, especially in the propeller slipstream, enabled to increase the accuracy of the numerical solution.

The multiphase VOF (Volume of Fluid) approach was coupled with the cavitation model for modelling the cavitation phenomena. For the convection term of the VOF approach, High-Resolution Interface Capturing (HRIC) was used to track the sharp interfaces between phases. The Schnerr-Sauer mass transfer model based on the reduced Rayleigh-Plesset equation was used to model the cavitation. In this model, the customisable cavitation parameters (i.e., nuclei density and diameter) were taken as default values based on our recent investigation of its effects on the sheet and tip vortex cavitation formation (Sezen and Atlar, 2021). Thus, the nuclei density and diameter were set to 10^{12} ($1/m^3$) and 10^{-6} (m), respectively.

The DES method was initialised with a steady-state RANS approach using the k-ω SST turbulence model. After initialising with the RANS method, the solver was switched to the DES method by activating the cavitation. When the flow field converged, the acoustic analogy was activated to collect the acoustic during the six propeller revolutions.

The Moving Reference Frame (MRF) technique was used to model the propeller rotational motion at the initialisation stage with the steady RANS method. When the solver was switched to the DES method, the propeller rotational motion technique was changed with the Rigid Body Motion (RBM). During the first propeller rotation, the timestep was set to 1° of propeller rotational rate and then was reduced to 0.5° of propeller rotational rate to avoid any possible stability issues by cavitation phenomena.

4. Results

4.1. Model scale

4.1.1. Hydrodynamic results

Table 3 shows the comparison of hydrodynamic performance characteristics between CFD, experiment and sea trial. Thrust and torque identity were applied separately during the experiments as the thrust and torque coefficients derived from sea trials do not correlate accurately with the propeller open water curve. Thus, in this study,

Table 3
Comparison of global performance characteristics between CFD, experiment and sea trial data for all operating conditions.

Condition	SEA-TRIAL AND EXPERIMENTS		CFD		Δ(%)	
	$10K_Q$ (sea-trial and experiment)	K_T (Sea-trial and experiment, from $10K_Q$)	K_T	$10K_Q$	K_T	$10K_Q$
C1	0.336	0.237	0.239	0.339	0.844	0.893
C2	0.318	0.221	0.236	0.340	6.787	6.918
C3	0.323	0.225	0.237	0.342	7.239	5.882
C4	0.318	0.221	0.237	0.346	5.333	8.805

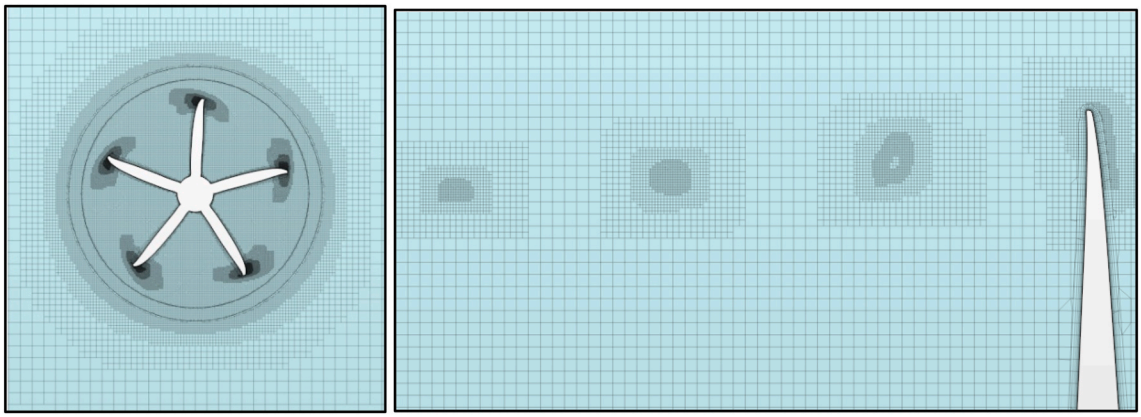

Fig. 4. Representation of grid resolution in the computational domain, permeable surface, and tip vortex areas.

experimental data obtained by torque identity was used to validate CFD results. The thrust coefficients are determined based on the torque coefficients using the open water characteristics of the propeller. In the CFD calculations, the torque identity was somewhat tried to replicate, but it could not be entirely done as it requires several iterations to find the equal torque values with the sea trial and experiment.

As shown in Table 3, the maximum difference between sea-trial and experiments is 8.805% in Condition 4, whereas the minimum difference is around 1% in Condition 1 for torque coefficient.

4.1.2. Cavitation observations

Figs. 5–8 show the comparison of cavitation extensions between CFD, experiment and sea trial data. The experimental figures were taken from Tani et al. (2019), whereas the sea-trial observations were taken from Sampson et al. (2015) for all operating conditions.

Fig. 5 shows the cavitation extension observed when the engine speed was 900 rpm (i.e., C1). The full-scale propeller cavitation mainly consists of leading-edge tip vortex cavitation. The relatively stable tip vortex cavitation, which is less intermittent, emanating from the blade's suction side, is present in full-scale. This stable leading-edge vortex cavitation extends through the propeller slipstream. Also, the cavitation dynamics seem to be experienced with bursting phenomena, as shown in Fig. 5. At C1, the model scale observations are characterised by the leading-edge vortex cavitation when the propeller passes at 0°, similar to the full-scale. Unlike the sea trials, the vortex cavitation is not persistent in the model scale. Compared to the sea trial and experiment, the relatively less leading-edge vortex cavitation is observed in the CFD calculations. As the vortex diameter is quite small, the CFD predictions could not capture the vortex cavitation as in the sea trial. Nevertheless, the cavitation observations on the blades obtained by CFD, experiment and sea-trial are similar, except for the leading-edge vortex cavitation in the propeller slipstream.

The cavitation observations are compared at 1200 rpm engine speed (i.e., C2) in Fig. 6. As shown in Fig. 6, with an increase in engine loading

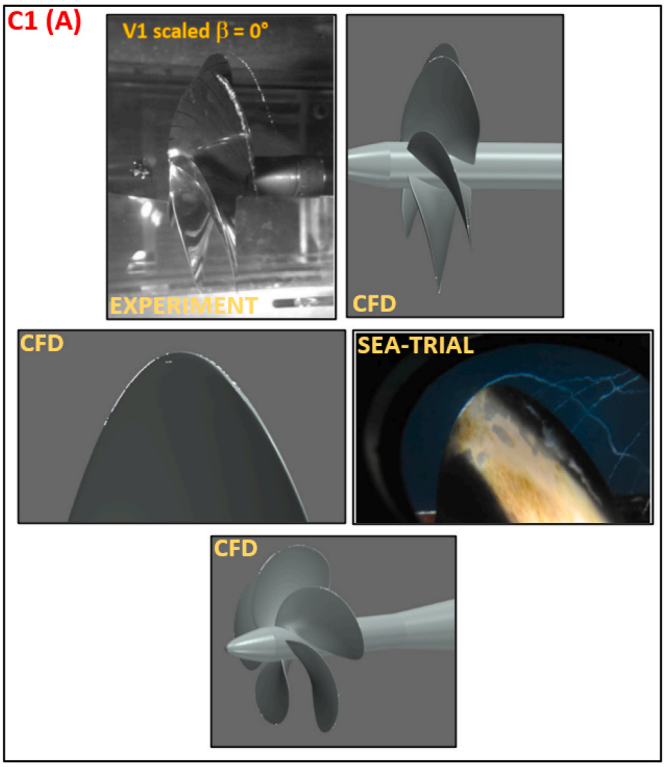

Fig. 5. Comparison of cavitation observations between CFD, experiment and sea-trial at C1 ($\alpha_v = 0.1$).

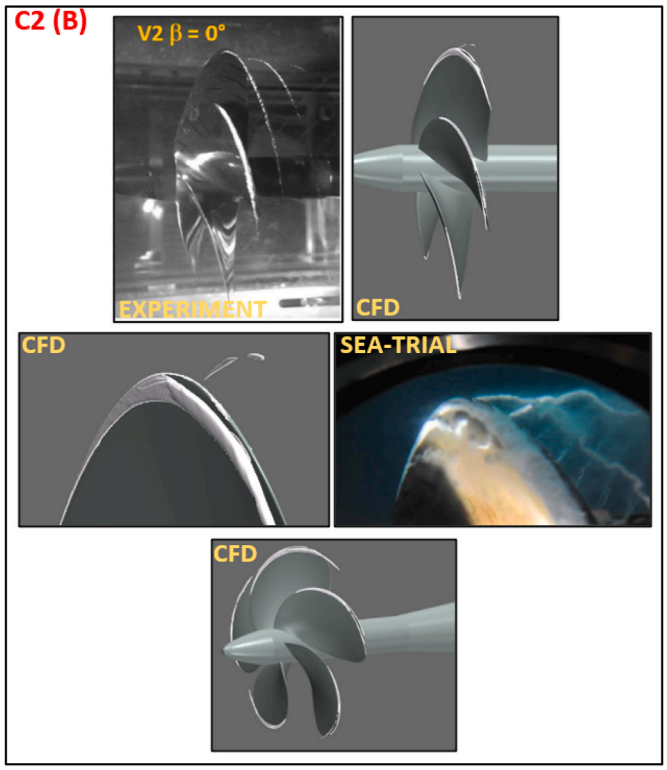

Fig. 6. Comparison of cavitation observations between CFD, experiment and sea-trial at C2 ($\alpha_v = 0.1$).

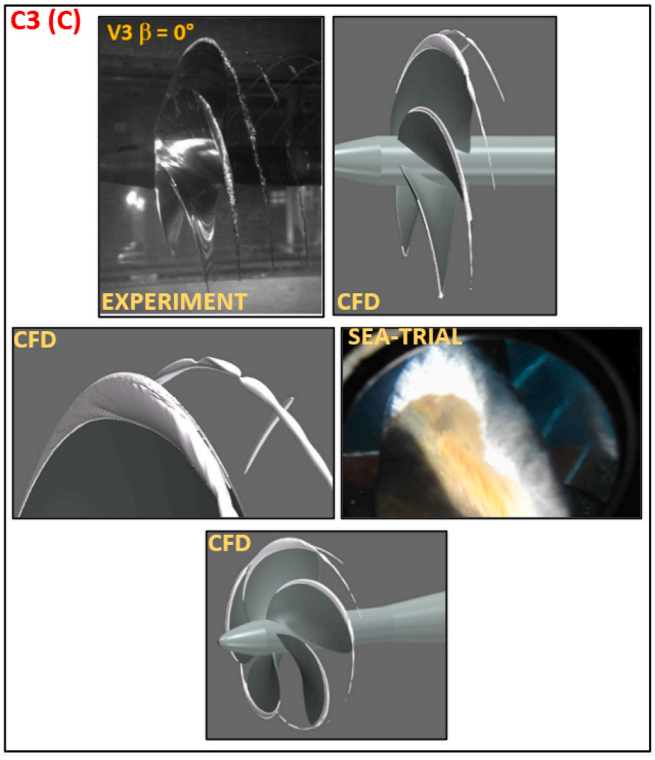

Fig. 7. Comparison of cavitation observations between CFD, experiment and sea-trial at C3 ($\alpha_v = 0.1$).

from 900 rpm to 1200 rpm, the strong suction side sheet cavitation appears on the blades in the full-scale. Also, the sheet cavitation breaks up partially and shedding bubble and vortex structures extending

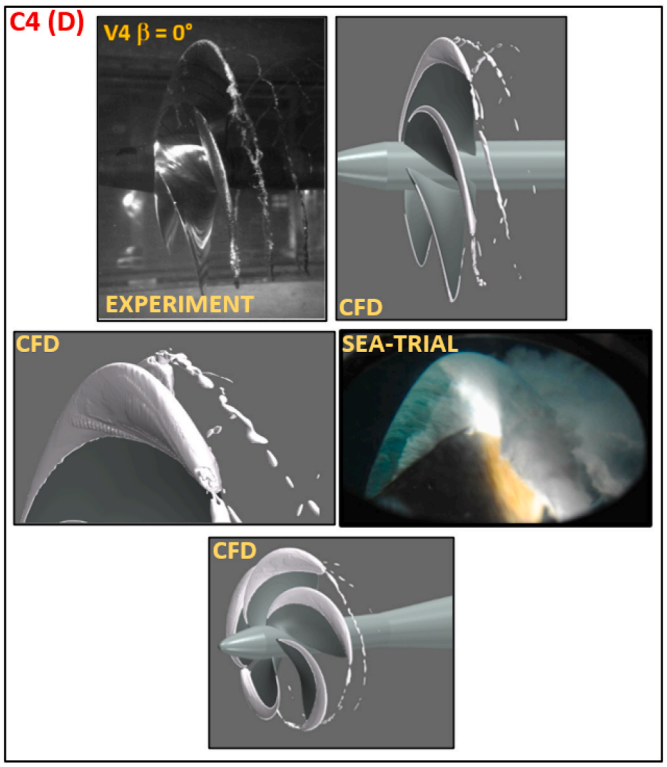

Fig. 8. Comparison of cavitation observations between CFD, experiment and sea-trial at C4 ($\alpha_v = 0.1$).

downstream of the propeller can be observed. The experiments and CFD predictions show the analogous feature of the cavitation, except for complex cavity structures. Contrary to the experiment, the sheet cavitation is observed at inner radii in the CFD calculations, similar to sea-trial observations. Both experiment and sea-trial observations show trailing vortices in the propeller slipstream, whereas the extension of vortices in the CFD is almost non-existent.

Looking at the other full-scale operating condition (i.e., 1500 rpm, C3) in Fig. 7, the cavitation structures vary considerably compared to the previous operating condition (i.e., Fig. 6). The sheet cavitation becomes unstable, and its volume, intensity and chordwise extension on the blades increase significantly. The unsteady structures concentrate at the blade tip where the roll-up mechanism terminates the sheet cavity, resulting in TVC formation. Similar to sea trials, the extension and volume of sheet cavitation increase in the experiment and CFD. The break-up of tip vortices is not present, and its diameter is clearly defined. The TVC extension in the propeller slipstream in the CFD is not as same as the model experiment and sea-trial data. This is because the V-AMR technique was applied inside the rotating region with reasonable extension to keep the computational cost reasonable. Also, the diameter of the TVC reduces further downstream and additional refinements with reduced mesh size might be required.

The cavitation extensions observed at the highest loading condition (i.e., C4) are given in Fig. 8. The cavitation volume and intensity increase rapidly at this operating condition, and the sheet cavitation covers approximately 25–30% of the blade. As shown in Fig. 8, the unsteady sheet cavitation and the cloudy formation are present. Like C2 and C3, the roll-up terminates the sheet cavitation at the propeller's blade tip, and thick, cloudy and unstructured TVC occurs and extends downstream of the propeller. The experiment and CFD calculations could not capture the cloudy appearance of the sheet and TVC as in the sea trial. Additionally, the coverage of sheet cavitation on the blades is underpredicted in the experiment and CFD compared to the sea-trial observations. Despite the lack of cloudy TVC dynamics observed in the experiment and CFD, the unstable behaviour of TVC dynamics is observed partially in comparison with the sea-trial data. The sheet cavitation is present at inner radii in the CFD, and overall cavitation volume seems to be higher in the CFD observations compared to the experiment.

4.1.3. URN predictions

4.1.3.1. Verification of the results. The verification study is generally conducted for hydrodynamic performance coefficients (e.g., thrust, torque and efficiency) for marine propellers using different grid spacing. According to the uncertainty of the numerical solution, the suitable grid spacing is found in the numerical calculations. However, the hydrodynamic and hydroacoustic solutions differ considerably. The hydrodynamic performance coefficients can be predicted accurately with relatively coarse grid numbers. In contrast, the hydroacoustic results are more dependent on grid resolution than the hydrodynamic solution, as shown in our recent study (Sezen et al., 2021b). The relatively coarse grids used in the hydrodynamic simulations are not suitable for the hydroacoustic part of the solution. This is because the insufficient grid resolution for the hydroacoustic part can create non-physical numerical noise and hence contaminate the overall acoustic pressure levels. Due to this fact, the verification of propeller URN predictions, which is the main interest of this study, can be carried out by comparing hydrodynamic and hydroacoustic results in the near-field (i.e., in the vicinity of the propeller and porous surface).

As stated in the introduction, an incompressible assumption (i.e., used for propeller hydrodynamic analysis) makes the sound speed infinite and hence denies sound propagation. Thus, it is not suitable for far-field noise estimations. However, the pressure collected at a specified location is not the resultant value, which contains all possible pressure waves travelling in the fluid due to the nondefined sources. Instead, the pressure is a rather instantaneous value as it occurs overlapping all nondefined sources' contributions at a certain location simultaneously. The time shift (i.e., compressibility delays) affects the overall signature of the pressure in terms of amplitude and waveform. Also, compressibility delays are dependent on relative motion between each noise source, measurement point and propagation speed. When the speed of sound underwater (around 1500 m/s) and the propeller's rotational rate is considered, the propeller's rotational speed is very low compared to propagation speed. Thus, this makes the time shifts negligible, and a comparison of both pressures in the near field is meaningful, as shown in the studies by (Ianniello et al., 2013; Sezen and Kinaci, 2019; Testa et al., 2021).

Fig. 9 and Table 4 show the location of the receivers and their coordinates, respectively. The NHP1 is positioned upstream of the propeller, whereas the NHP3 is located downstream of the propeller. The NHP2 is located at the propeller plane. The origin of the coordinates is defined as the centre of the propeller blades.

Figs. 10 and 11 show the hydrodynamic and hydroacoustic pressures computed at the C1 (i.e. 900 rpm) and C2 (i.e., 1200 rpm) loading conditions, respectively, for three receivers located in the vicinity of the propeller. In the near field, the overall pressures are mainly characterised by BPF (Blade Passage Frequency) for C1 and C2. For both operating conditions, the contribution of linear noise sources to the overall acoustic pressure level is dominant, particularly for NHP1 and NHP2. Further downstream (i.e., NHP3), the contribution of nonlinear sources coming from the propeller slipstream can start to appear. Hence, the pressure increases with respect to the receiver located upstream of the propeller (i.e., NHP1) though their locations from the noise source are quite similar. The maximum hydrodynamic and hydroacoustic pressures are computed at NHP2 as it is located at the propeller plane, where the distance is reduced from the noise source compared to NHP1 and NHP3. As shown in the previous section, the considerable increase in cavitation volume increases pressure levels from C1 to C2 for each

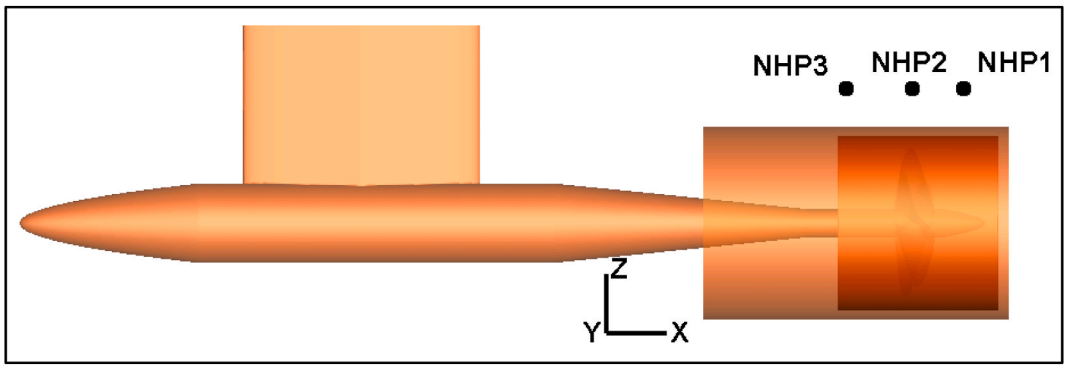

Fig. 9. Representation of receivers around the porous region (Figure is not scaled).

Table 4
Receiver coordinates.

Receiver	X (m)	Y (m)	Z (m)
NHP1	0.05	0	0.171
NHP2	0	0	0.171
NHP3	−0.06	0	0.171

receiver. The agreement between both pressures at each receiver location shows the accuracy of the hydrodynamic and hydroacoustic solutions.

4.1.3.2. Comparison of numerical results with the measurements. The noise measurements were conducted in the UNIGE using three different receivers, as shown in Fig. 12. Two receivers were attached on fins downstream with respect to the propeller. Receiver H2 was placed portside at the same vertical direction of the propeller shaft, while the receiver H3 was placed on starboard at a lower vertical position. Also, the receiver HP1 is mounted in an external plexiglass tank filled with water and mounted on the test section's bottom window. The noise measurements were performed by taking the ITTC, 2017b guideline into account for analysing the data. The measured noise levels were corrected at 1m using the transfer functions to eliminate confined environment effects. The Source Strength Levels (SL) were computed from the measured Sound Pressure Levels (SPL), and noise spectrums were

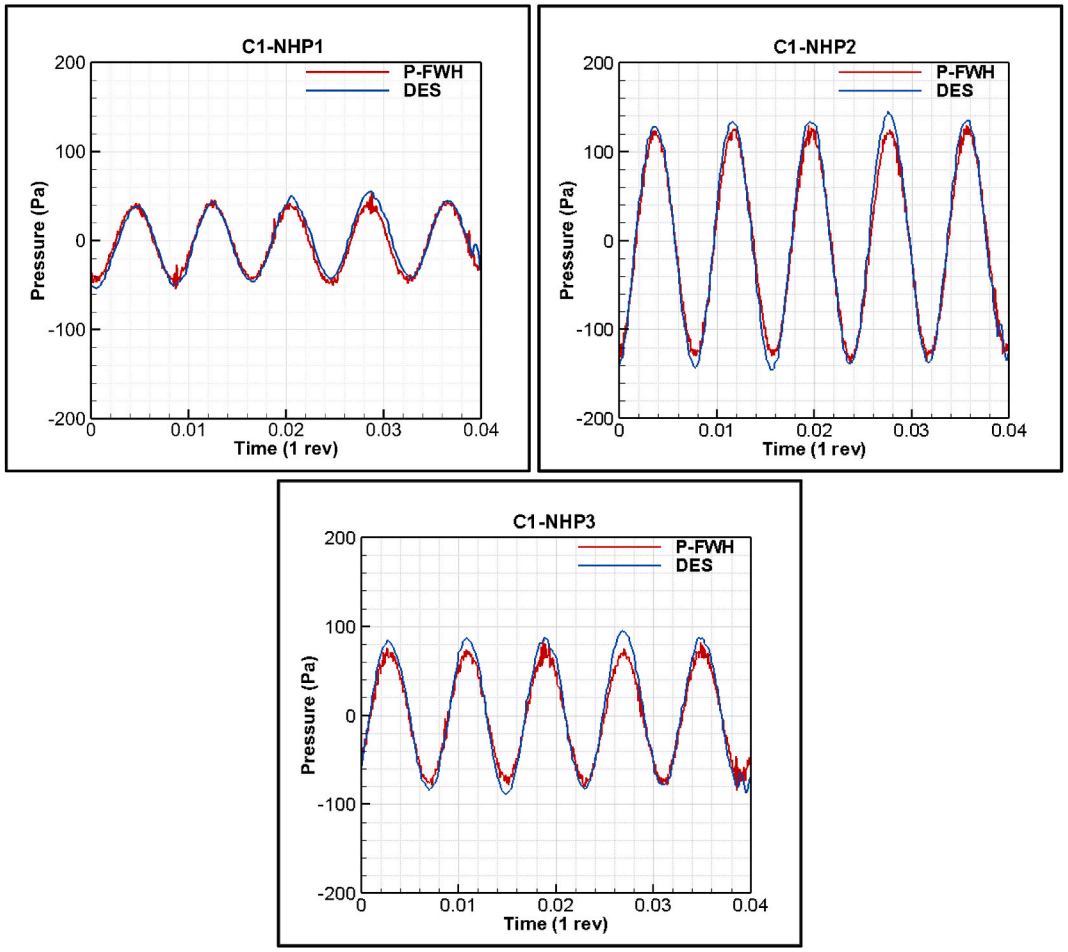

Fig. 10. Comparison of hydrodynamic and hydroacoustic pressures at C1 for three receivers located in the near-field.

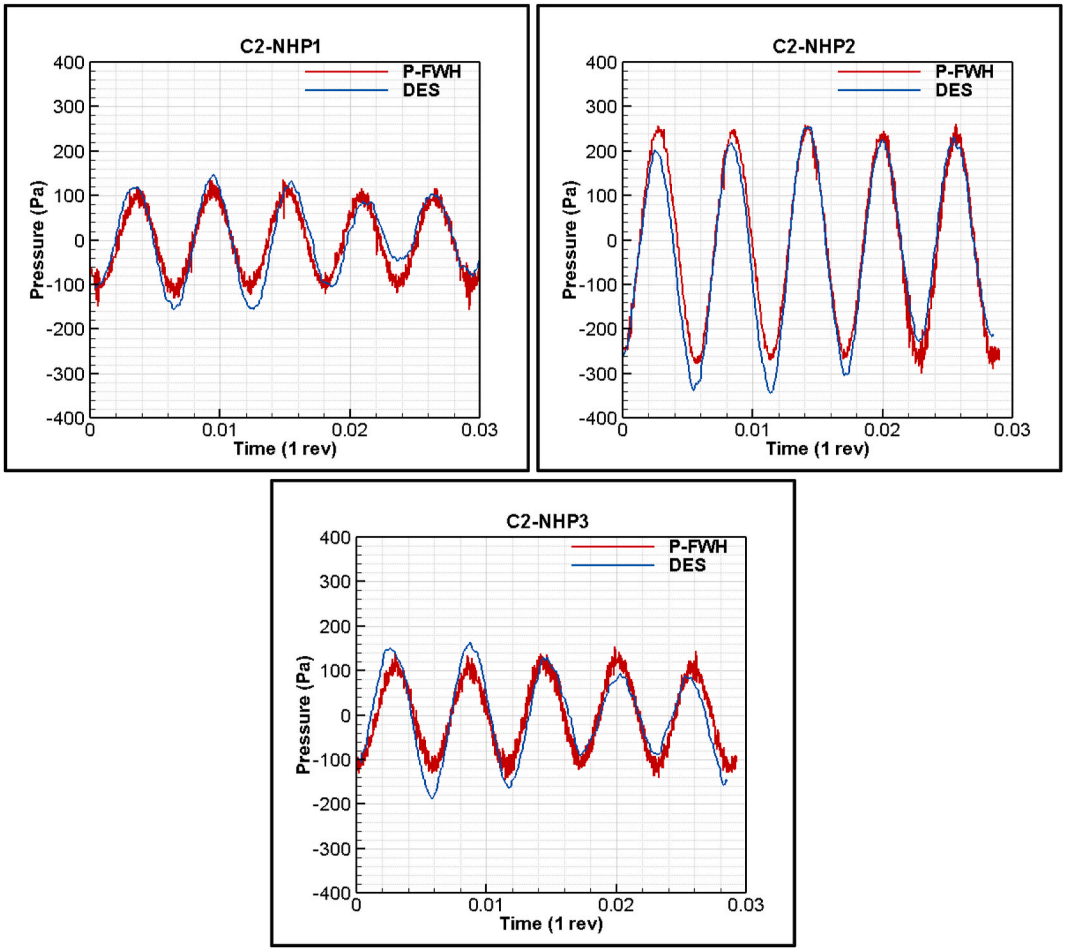

Fig. 11. Comparison of hydrodynamic and hydroacoustic pressures at C2 for three receivers located in the near-field.

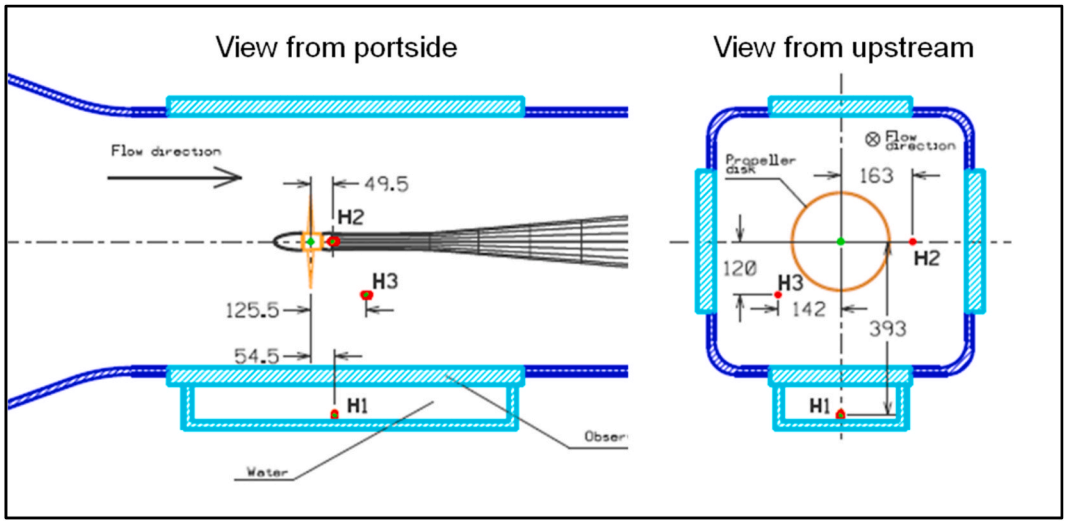

Fig. 12. The receiver locations for the URN measurements during the experiments in UNIGE (Tani et al., 2017).

derived in one-third octave (OTO).

Similar to the experiment setup, three receivers were placed at the same locations in the CFD computations. Additionally, one more receiver was located at the propeller plane, where the distance between the noise source and receiver was set to 1m as a reference distance defined by ITTC, 2017b. As the transfer functions were not available from the experiments, the spherical spreading loss definition (i.e., $20\log(d/d_{ref})$) was utilised as a transfer function to extrapolate the results from the receivers to reference distance (i.e., 1m) to compute the SL in the CFD computations.

The noise predictions were carried out using only receiver H1, and then the measured levels were extrapolated to reference distance in the

experiment to obtain the noise spectra in the model scale. Thus, akin to the experiment, only receiver H1 was utilised in the CFD calculations to compare the predictions with the measurements at different operating conditions.

Fig. 13 compares predicted URN levels with the measured data in the cavitation tunnel at four different operating conditions. The general comments regarding the comparison between CFD and the experiment can be summarised.

- In the measured data, there is a peak of around 740Hz related to the vibration of receiver support during the measurements. As the magnitude of this component becomes higher when the propeller is fitted inside the tunnel, it could not be eliminated during the background measurements as described in Tani et al. (2017). This peak can also overlap with the spectral hump created by tip vortex dynamics at the medium-low frequency region of the noise spectrum at some operating conditions. Details of the measurements can be found in the study by Tani et al. (2017) and Tani et al. (2019).
- The CFD predictions agree with the measured data, particularly at C1, C2 and C3. . However, unlike these conditions, the propeller URN levels are overpredicted up to 10 dB between 1 kHz and 4 kHz using CFD compared to measured data at C4. This can be because of the larger sheet cavitation observed in the CFD than in experimental observations.
- There is a discrepancy around 1 kHz between CFD and experiment for all operating conditions. This deviation seems to be because of the vibration of receiver support during the measurements, as explained above.
- The URN levels predicted by CFD using the receiver located at 1m and shifted to 1m using the HP1 together with the ITTC distance normalisation show similar values as the near-field effects are not present at HP1 compared to HP2 and HP3.
- C2, C3 and C4 conditions slightly show a spectral hump in the CFD predictions due to the TVC modelled using the V-AMR technique between 400Hz and 1 kHz, similar to experiments.
- The 1st BPF value is well predicted in the CFD predictions for all operating conditions.
- More extended cavitation is seen on and off the blade with increased engine loading. This resulted in increased URN levels from C1 to C4.

4.2. URN predictions in full scale

The sea trials for the Princess Royal vessel were carried out to measure the URN in full-scale in the scope of the SONIC project at different operating conditions, and comprehensive database were created (SONIC, 2012). During the sea trials, different receiver arrays were utilised by SOTON and CETENA and data was presented both in narrowband and OTO. Hence, the numerical results were compared with the full-scale data collected by CETENA and SOTON in this study. The details of the full-scale measurements conducted by SOTON can be found in Brooker and Humphrey (2014); Brooker and Humphrey (2016); Humphrey and Brooker (2019).

The measured noise data in the cavitation tunnel were extrapolated to full-scale using the ITTC procedure (ITTC, 2017b). The frequency scaling between model and full-scale is given as follows.

$$\frac{f_s}{f_m} = \frac{n_s}{n_m}\cdot\sqrt{\frac{\sigma_s}{\sigma_n}} \tag{3}$$

An increase in Sound Pressure Level (SPL) in full-scale is given as:

$$\Delta SPL = 20\log\left[\left(\frac{\sigma_s}{\sigma_n}\right)^{w}\left(\frac{r_m}{r_s}\right)^{x}\left(\frac{n_s D_s}{n_m D_m}\right)^{y}\left(\frac{D_s}{D_m}\right)^{z}\right] \tag{4}$$

Here, the subscripts s and m refer to full-scale and model scale propellers, respectively. r is the distance between the noise source and receiver. In this procedure, two sets of parameters (w, x, y, z) can be used

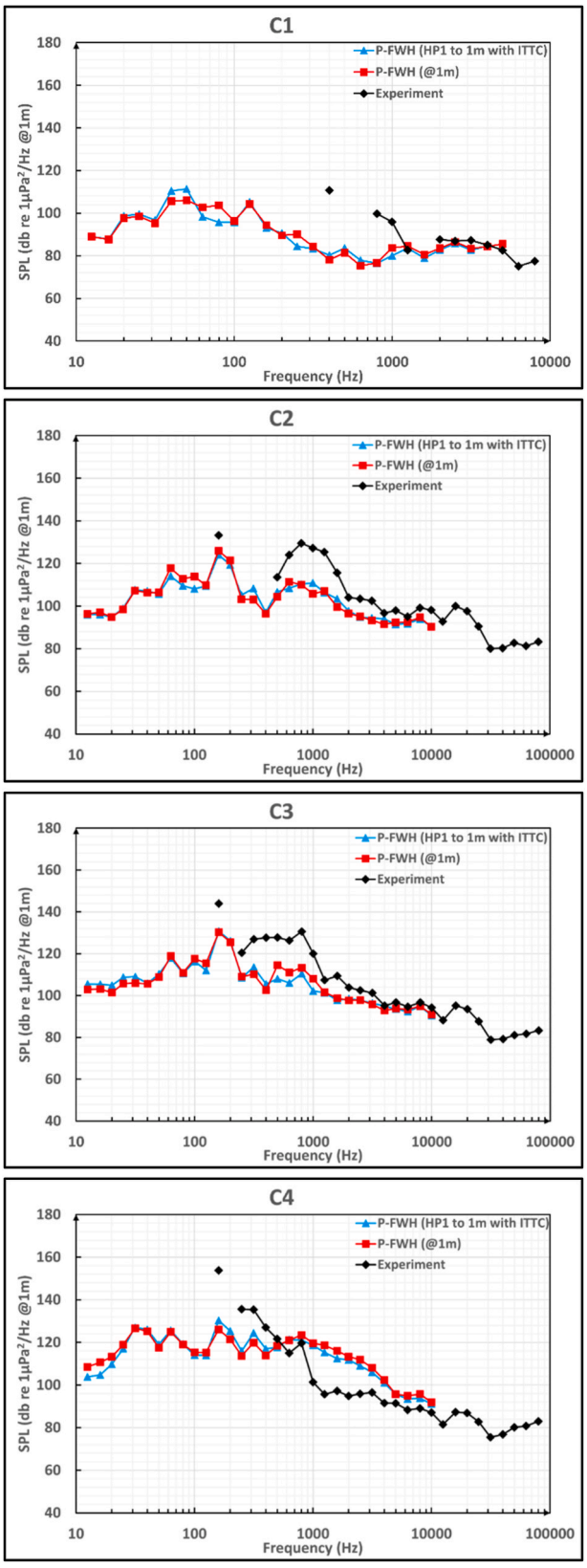

Fig. 13. Comparison of predicted URN levels with measured data at C1, C2, C3 and C4 in model scale.

for the extrapolation, and the selection of parameters is dependent on the variation of acoustic efficiency. The high-frequency formulation is based on constant efficiency assumption, whereas the low-frequency formulation is used when the acoustic efficiency is proportional to the Mach number (ITTC, 2017b). As stated in Tani et al. (2019), the tip vortex showed oscillating behaviour during the cavitation tunnel tests, and hence this oscillating behaviour was considered to be more dominant than bubble collapse. Thus, the low-frequency formulation was applied using the exponents in Table 5 for both the constant and proportional bandwidth of the noise spectra. It should be noted that the full-scale noise spectra are derived using the average of three receivers shown in Fig. 12. Similar to experiments, the same procedure was followed to extrapolate predicted noise levels from the model to full-scale using CFD. The noise spectrums are given in OTO band representation in full-scale at 1m, and spectra are presented as Power Spectral Density (Pa^2/Hz).

Fig. 14 shows the comparison of extrapolated results using the CFD and experiment with the full-scale measurements performed by SOTON and CETENA. As shown in Fig. 14, the numerical results are extrapolated to full-scale using both the average of three receivers and the receiver located directly at 1m. The numerical results underpredicted the URN levels between 5 dB and 30 dB at certain frequencies compared to sea trials at C1. According to cavitation extensions, the weak leading-edge vortex cavitation, which extends in the propeller slipstream, is observed during the sea trials. However, in the CFD calculations, this TVC could not be observed, including possible bursting phenomena (see Fig. 5). Thus, the lack of leading-edge vortex cavitation dynamics captured in the CFD calculations and many other scale factors can cause the differences between predicted and measured URN levels at full-scale. Similar to CFD predictions, the URN levels are underpredicted up to 10 dB using the extrapolated measured data obtained by the cavitation tunnel measurements at certain frequencies. The 1st BPF value was captured in the CFD calculations in the low-frequency region of the noise spectrum. The extrapolated data at 1m using the average of three receivers and the receiver located directly at 1m show a different behaviour, particularly until 1 kHz. The reason can be because the near-field effects are more dominant at receivers H2 and H3 than H1. Thus, the dominant near field effects for H2 and H3 characterise the receivers' average, particularly when the cavitation is not strong, resulting in a noise difference compared to the receiver located directly at 1m.

Fig. 15 compares CFD predictions, cavitation tunnel measurements and full-scale measurements in full-scale at C2. As shown in Fig. 15, the discrepancy between the CFD prediction and full-scale measurements is around 15 dB between approximately 100Hz and 3 kHz at C2. The complex cavity dynamics, including break-up phenomena and TVC extension in the propeller slipstream, could not be observed in the CFD calculations, although similar sheet cavitation extensions are present between CFD, experiment and full-scale observations (see Fig. 6). Therefore, these dissimilarities between the CFD predictions and full-scale observations are probably the main reason for the URN difference. The extrapolated data using the tunnel measurements show that URN levels are underpredicted in full-scale compared to sea-trial data. Nevertheless, the extrapolated data using the tunnel measurements are closer to the full-scale measurements than those of extrapolated data based on CFD predictions.

Similar to C2, the measured full-scale URN levels are higher than those of extrapolated URN levels using CFD at C3, as shown in Fig. 16. The discrepancy of URN levels is around 10 dB between both approaches. Akin to the previous conditions, the numerical calculations underpredicted the URN levels up to 15 dB compared to full-scale measurements at C3, as shown in Fig. 16. The unstable sheet cavitation with the cloudy formation and periodic vortex break up phenomenon is not present in CFD observations. Hence, this lack of cavitation dynamics leads to the URN differences between the CFD and full-scale measurements.

The last comparison between the CFD, tunnel measurements and sea-trial data is carried out at the highest loading condition (i.e., C4) in Fig. 17. Unlike the other operating conditions (i.e., C1, C2 and C3), the numerical predictions are in good agreement with the full-scale measurements up to around 2 kHz. Akin to the other operating conditions, the 1st BPF value was well captured in the CFD. The numerical results show sudden decay after 2 kHz. The reason is that the strong TVC dynamics observed during the sea trials at C4 and these dynamics can dominate the broadband part of the noise spectrum. Also, the interaction between sheet and TVC is rather complex at C4. Thus, the lack of reproduction of cavity dynamics and their interactions can cause the underprediction of URN levels after 2 kHz.

The underprediction of propeller URN levels between the sea trial and extrapolated data based on CFD predictions can also be related to different flow field modelling and, hence, the Reynolds number. This different flow field between the model and full-scale propeller inevitably affects the cavitation dynamics; hence, the propeller URN. This can be further related to the interaction between the hull and propeller, which is not present in the present case.

Table 5
Exponents for the low-frequency formulation.

Bandwidth	w	x	y	z
Constant	0.75	1	1.5	1.5
Proportional	1	1	2	1

5. Conclusion

This study presented hydrodynamic performance, cavitation extension and URN of the benchmark propeller operating under non-uniform flow conditions. The cavitating flow around the propeller and URN predictions were performed using DES and permeable formulation of the FWH equation. The numerical results were first validated with the experimental and sea trial data through the propeller hydrodynamic performance characteristics and cavitation extensions. Then, the numerical results were verified by comparing the hydrodynamic and hydroacoustic pressures in the near field. The noise predictions were validated with the cavitation tunnel measurements. Finally, the obtained URN results were extrapolated to full-scale with the aid of ITTC extrapolation procedures and validated with the extrapolated measured data in the cavitation tunnel and full-scale measurements. The crucial findings of this study can be summarised as follows.

- The propeller hydrodynamic performance characteristics (i.e., thrust and torque) were found in good agreement compared to experiments and sea trial data, except highest loading conditions. The minimum and maximum difference between the CFD and sea trial data was computed at around 9% and 1%, respectively.
- The cavitation extensions, particularly sheet cavitation, were generally predicted to be similar under non-uniform flow conditions, except for the highest loading condition, as in the experiment and sea trial observations. However, as expected, the strong cavity dynamics as in the sea trail could not be observed in the CFD, and it led to the discrepancy of URN levels between CFD and full-scale measurements.
- The proposed V-AMR technique successfully modelled the TVC in the propeller slipstream, provided the TVC diameter is relatively big. Yet, when the weak or intermittent TVC was present, the V-AMR technique could not capture the TVC in the propeller slipstream. The reason is that the adopted grid resolution inside the vortex seems to be not sufficient enough to capture weak and intermittent TVC in the propeller slipstream.
- The hydroacoustic results were verified by comparing the hydrodynamic and hydroacoustic pressures in the near field. Thus, the consistency and accuracy of the solution were shown using the receivers

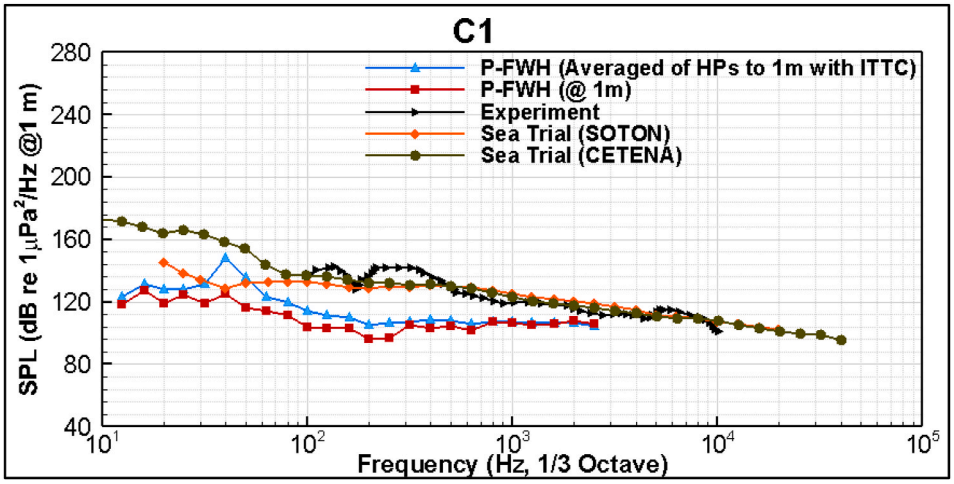

Fig. 14. Comparison of predicted noise levels using CFD, measured data using the cavitation tunnel with full-scale measurements at URN at C1 in full-scale.

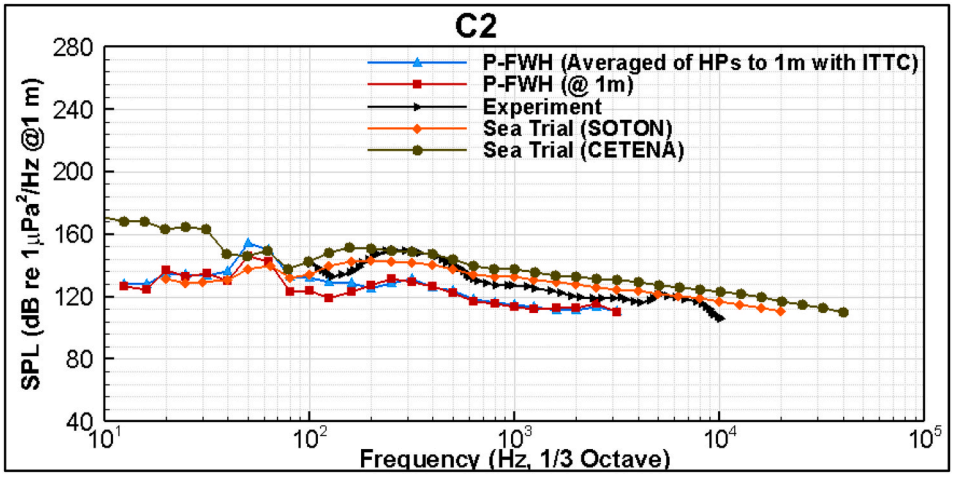

Fig. 15. Comparison of predicted noise levels using CFD, measured data using the cavitation tunnel with full-scale measurements at URN at C2 in full-scale.

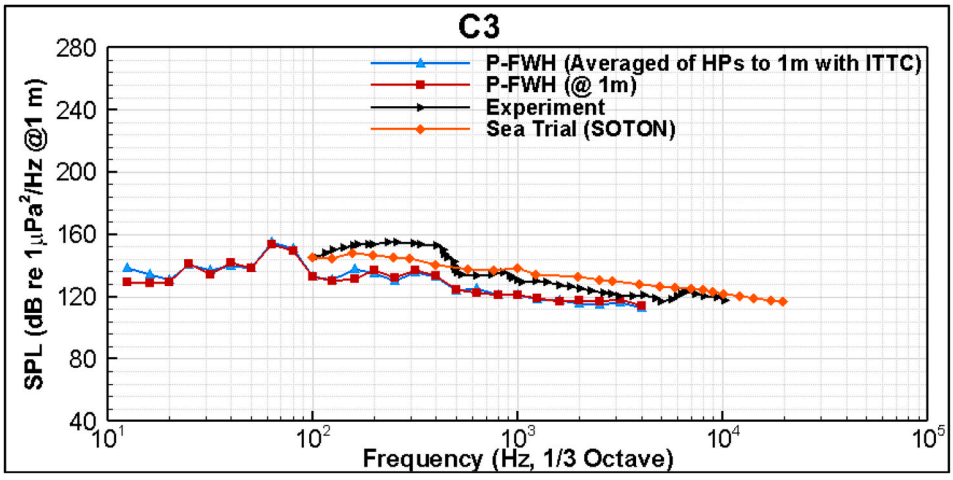

Fig. 16. Comparison of predicted noise levels using CFD, measured data using the cavitation tunnel with full-scale measurements at URN at C3 in full-scale.

located in the proximity of the permeable surface under non-uniform flow conditions.

- The propeller URN predictions were found in line with the cavitation observations. Also, the numerical calculations showed good agreement with the measured data under non-uniform flow conditions, except at the highest loading condition. This can be associated with the large extension of sheet cavitation observed in the CFD,

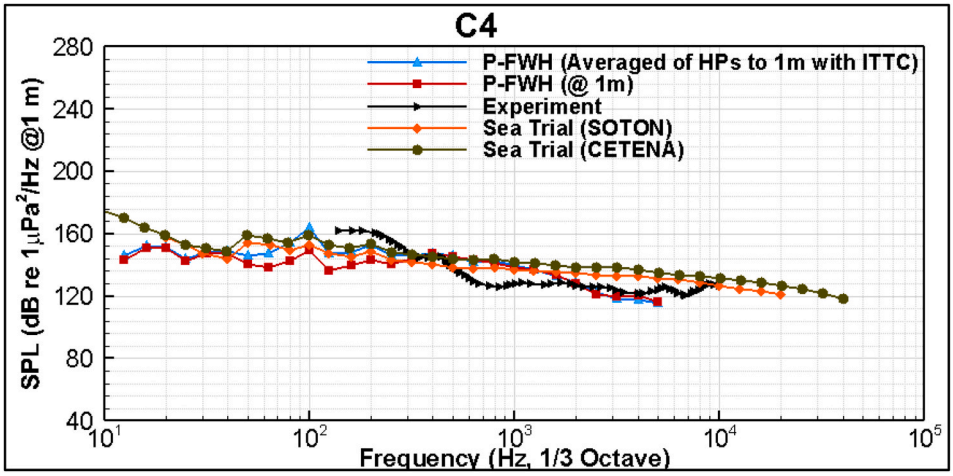

Fig. 17. Comparison of predicted noise levels using CFD, measured data using the cavitation tunnel with full-scale measurements at URN at C3 in full-scale.

which led to overprediction of propeller URN levels between 1 kHz and 10 kHz compared to the measured data.

- The extrapolated propeller URN predictions were compared with the full-scale measurements under non-uniform flow conditions. The maximum discrepancy was observed at the lowest loading condition due to the lack of possible bursting phenomenon in the CFD compared to the full-scale measurements. In general, the propeller URN was underpredicted by around 10 and 15 dB in the numerical calculations compared to full-scale measurements. At the highest loading condition, the predictions were in good agreement with the full-scale measurements.
- The present research study was carried out using the numerical methods based on incompressibility assumption. Thus, as a future study, the numerical investigations will be extended using the numerical methods based on compressibility assumption to explore the possible differences between two approaches in terms of propeller URN.

CRediT authorship contribution statement

Savas Sezen: Conceptualization, Methodology, Software, Validation, Investigation, Resources, Data curation, Writing – original draft, Writing – review & editing, Visualization. **Mehmet Atlar:** Investigation, Resources, Data curation, Writing – original draft, Writing – review & editing, Supervision, Project administration.

Declaration of competing interest

The authors declare that they have no known competing financial interests or personal relationships that could have appeared to influence the work reported in this paper.

Data availability

No data was used for the research described in the article.

Acknowledgements

The first author was sponsored by Stone Marine Propulsion Ltd of the UK and the University of Strathclyde during his PhD study. Results were obtained using the ARCHIE-WeSt High-Performance Computer (www.archie-west.ac.uk) based at the University of Strathclyde. The authors also thank Dr Giorgio Tani for providing the experimental data.

Abbreviations

URN	Underwater Radiated Noise
V-AMR	Vorticity-based Adaptive Mesh Refinement
TVC	Tip Vortex Cavitation
ITTC	International Towing Tank Conference
IMO	International Maritime Organisation
CIS	Cavitation Inception Speed
CFD	Computational Fluid Dynamics
DNS	Direct Numerical Simulation
LES	Large Eddy Simulation
DES	Detached Eddy Simulation
RANS	Reynolds-averaged Navier-Stokes
DDES	Delayed Detached Eddy Simulation
FWH	Ffowcs Williams Hawkings
SST	Shear Stress Transport
RR	Round Robin
UNIGE	University of Genoa
LDV	Laser Doppler Velocimetry
CFL	Courant–Friedrichs–Lewy
VOF	Volume of Fluid
HRIC	High-Resolution Interface Capturing
MRF	Moving Reference Frame
RBM	Rigid Body Motion
SONIC	Suppression Of underwater Noise Induced by Cavitation
OTO	One-third Octave

References

Aktas, B., Atlar, M., Turkmen, S., Korkut, E., Fitzsimmons, P., 2016a. Systematic cavitation tunnel tests of a Propeller in uniform and inclined flow conditions as part of a round robin test campaign. Ocean. Eng. 120, 136–151. https://doi.org/10.1016/j.oceaneng.2015.12.015.

Aktas, B., Atlar, M., Turkmen, S., Shi, W., Sampson, R., Korkut, E., Fitzsimmons, P., 2016b. Propeller cavitation noise investigations of a research vessel using medium size cavitation tunnel tests and full-scale trials. Ocean. Eng. 120, 122–135. https://doi.org/10.1016/j.oceaneng.2015.12.040.

Asnaghi, A., Svennberg, U., Bensow, R.E., 2020. Large Eddy Simulations of cavitating tip vortex flows. Ocean. Eng. 195, 106703 https://doi.org/10.1016/J.OCEANENG.2019.106703.

Atlar, M., Aktas, B., Samspon, R., Fitzsimmons, P., Fetherstonhaug, C., 2013. A multi-purpose marine science and technology research vessel for full-scale observations and measurements. In: 3rd International Conference on Advanced Model Measurement Technologies for the Marine Industry, AMT'13. Gdansk, Poland.

Bensow, R.E., Liefvendahl, M., 2016. An acoustic analogy and scale-resolving flow simulation methodology for the prediction of propeller radiated noise. In: 31st Symposium on Naval Hydrodynamics. Monterey, California, USA, pp. 1–19.

Breeze, H., Nolet, V., Thomson, D., Wright, A.J., Marotte, E., Sanders, M., 2022. Efforts to advance underwater noise management in Canada: introduction to the marine pollution bulletin special issue. Mar. Pollut. Bull. 178, 113596 https://doi.org/10.1016/J.MARPOLBUL.2022.113596.

Brooker, A., Humphrey, V., 2016. Measurement of radiated underwater noise from a small research vessel in shallow water. Ocean. Eng. 120, 182–189. https://doi.org/10.1016/j.oceaneng.2015.09.048.
Brooker, A., Humphrey, V., 2014. Measurement of radiated underwater noise from a small research vessel in shallow water. In: A. Yücel Odabaşı Colloquium Series 1st International Meeting on Propeller Noise and Vibration. Istanbul, Turkey.
Di Francescantonio, P., 1997. A new boundary integral formulation for the prediction of sound radiation. J. Sound Vib. 202, 491–509. https://doi.org/10.1006/jsvi.1996.0843.
Erbe, C., Marley, S.A., Schoeman, R.P., Smith, J.N., Trigg, L.E., Embling, C.B., 2019. The effects of ship noise on marine mammals—a review. Front. Mar. Sci. 6, 606. https://doi.org/10.3389/FMARS.2019.00606.
Farassat, F., 2007. Derivation of formulations 1 and 1A of Farassat. In: NASA/TM-2007-214853, pp. 1–25.
Ffowcs Williams, J., 1992. Noise source mechanisms. In: Modern Methods in Analytical Acoustics. Lecture Notes. Springer, Berlin, pp. 313–354.
Ffowcs Williams, J.H., Hawkings, D.L., 1969. Sound generation by turbulence and surfaces in arbitrary motion. Philos. Trans. R. Soc. London. Ser. A, Math. Phys. Sci. 264, 321–342. https://doi.org/10.1098/rsta.1969.0031.
Fujiyama, K., Nakashima, Y., 2017. Numerical prediction of acoustic noise level induced by cavitation on ship propeller at behind-hull condition. In: Proceedings of the Fifth International Symposium on Marine Propulsors, SMP'17. Espoo, Finland.
Hallander, J., Li, D.-Q., Allenstrom, B., Valdenazzi, F., Barras, C., 2012. Predicting underwater radiated noise due to a cavitating propeller in a ship wake. In: Proceedings of the 8th International Symposium on Cavitation - CAV2012. Singapore, pp. 1–7.
Humphrey, V.F., Brooker, A., 2019. Variability of radiated underwater noise measurements for a small research vessel in shallow water. J. Acoust. Soc. Am. 146 https://doi.org/10.1121/1.5137625, 3061–3061.
Ianniello, S., De Bernardis, E., 2015. Farassat's formulations in marine propeller hydroacoustics. Int. J. Aeroacoustics 14, 87–103.
Ianniello, S., Muscari, R., Di Mascio, A., 2013. Ship underwater noise assessment by the acoustic analogy. Part I: nonlinear analysis of a marine propeller in a uniform flow. J. Mar. Sci. Technol. 18, 547–570. https://doi.org/10.1007/s00773-013-0227-0.
Ikeda, T., Enomoto, S., Yamamoto, K., Amemiya, K., 2017. Quadrupole corrections for the permeable-surface Ffowcs Williams–Hawkings equation. AIAA 55, 2307–2320. https://doi.org/10.2514/1.J055328.
IMO, 2014. MEPC.1/Circ.833: Guidelines for the Reduction of Underwater Noise from Commercial Shipping to Address Adverse Impacts on Marine Life.
ITTC, 2017a. The Specialist Committee on Hydrodynamic Noise, Final Report and Recommendations to the 28th ITTC-Volume II. Wuxu, China.
ITTC, 2017b. Model-Scale Propeller Cavitation Noise Measurements 7.5-02-01-05.
Korkut, E., Takinaci, A.C., 2013. 18M Research Vessel Wake Measurements, Faculty of Naval Architecture and Ocean Engineering. Istanbul Technical University, Istanbul, Turkey.
Leaper, R., Renilson, M., Ryan, C., 2014. Reducing underwater noise from large commercial ships: current status and future directions. J. Ocean Technol. 9, 51–69.
Li, D.-Q., Hallander, J., Johansson, T., Karlsson, R., 2015. Cavitation dynamics and underwater radiated noise signature of a ship with a cavitating propeller. In: VI International Conference on Computational Methods in Marine Engineering MARINE 2015. Rome, Italy.
Lidtke, A.K., Lloyd, T., Vaz, G., 2019. Acoustic modelling of a propeller subject to non-uniform inflow. In: Sixth International Symposium on Marine Propulsors, SMP'2019. Rome, Italy.
Lloyd, T.P., Rijpkema, D.R., van Wijngaarden, E., 2015. Propeller acoustic modelling: comparing CFD results with an acoustic analogy approach. In: Proceedings of the 4th International Symposium on Marine Propulsors. Austin, Texas, USA.
Muzaferija, S., Papoulias, D., Peric, M., 2017. VOF simulations of hydrodynamic cavitation using the asymptotic and classical Rayleigh-Plesset models. In: Fifth International Symposium on Marine Propulsion, Smp'17. Espoo, Finland.
Nitzkorski, Z., 2015. A Novel Porous Ffowcs-Williams and Hawkings Acoustic Methodology for Complex Geometries. Faculty of the Graduate School of the University of Minnesota. PhD thesis.
Nowacek, D.P., Thorne, L.H., Johnston, D.W., Tyack, P.L., 2007. Responses of cetaceans to anthropogenic noise. Mamm Rev. 37, 81–115. https://doi.org/10.1111/j.1365-2907.2007.00104.x.
Sampson, R., Turkmen, S., Aktas, B., Shi, W., Fitzsimmons, P., Atlar, M., 2015. On the full scale and model scale cavitation comparisons of a Deep-V catamaran research vessel. In: Fourth International Symposium on Marine Propulsors, SMP'15. Austin, Texas, USA.
Schnerr, G.H., Sauer, J., 2001. Physical and numerical modeling of unsteady cavitation dynamics. In: 4th International Conference on Multiphase Flow. New Orleans, USA.
Sezen, S., Atlar, M., 2021. An alternative Vorticity based Adaptive Mesh Refinement (V-AMR) technique for tip vortex cavitation modelling of propellers using CFD methods. Ship Technol. Res. 69, 1–21. https://doi.org/10.1080/09377255.2021.1927590.
Sezen, S., Atlar, M., Fitzsimmons, P., 2021a. Prediction of cavitating propeller underwater radiated noise using RANS & DES-based hybrid method. Ships Offshore Struct. 16, 93–105. https://doi.org/10.1080/17445302.2021.1907071.
Sezen, S., Atlar, M., Fitzsimmons, P., Sasaki, N., Tani, G., Yilmaz, N., Aktas, B., 2020. Numerical cavitation noise prediction of a benchmark research vessel propeller. Ocean. Eng. 211, 107549 https://doi.org/10.1016/j.oceaneng.2020.107549.
Sezen, S., Cosgun, T., Yurtseven, A., Atlar, M., 2021b. Numerical investigation of marine propeller Underwater Radiated Noise using acoustic analogy part 1: the influence of grid resolution. Ocean. Eng. 220, 108448 https://doi.org/10.1016/j.oceaneng.2020.108448.
Sezen, S., Kinaci, O.K., 2019. Incompressible flow assumption in hydroacoustic predictions of marine propellers. Ocean. Eng. 186 https://doi.org/10.1016/j.oceaneng.2019.106138.
Slabbekoorn, H., Bouton, N., van Opzeeland, I., Coers, A., ten Cate, C., Popper, A.N., 2010. A noisy spring: the impact of globally rising underwater sound levels on fish. Trends Ecol. Evol. 25, 419–427. https://doi.org/10.1016/J.TREE.2010.04.005.
SONIC, 2012. Suppression of underwater noise induced by cavitation. EC-FP7, Grant Agreement No: 2012 314394.
Spalart, P.R., Jou, W.-H., Strelets, M., Allmaras, S.R., Research, U.S.A.F.O. of S, 1997. Comments on the feasibility of LES for Wings, and on a hybrid RANS/LES approach. In: First AFOSR International Conference on DNS/LES. Greyden Press, pp. 137–148.
Star CCM + 14.06, 2019. User Guide, Siemens.
Stark, C., Shi, W., 2021. Hydroacoustic and hydrodynamic investigation of bio-inspired leading-edge tubercles on marine-ducted thrusters. R. Soc. Open Sci. 8, 210402 https://doi.org/10.1098/RSOS.210402.
Tani, G., Aktas, B., Viviani, M., Atlar, M., 2017. Two medium size cavitation tunnel hydroacoustic benchmark experiment comparisons as part of a round robin test campaign. Ocean. Eng. 138, 179–207. https://doi.org/10.1016/j.oceaneng.2017.04.010.
Tani, G., Aktas, B., Viviani, M., Yilmaz, N., Miglianti, F., Ferrando, M., Atlar, M., 2019. Cavitation tunnel tests for "The Princess Royal" model propeller behind a 2-dimensional wake screen. Ocean. Eng. 172, 829–843. https://doi.org/10.1016/j.oceaneng.2018.11.017.
Tani, G., Viviani, M., Felli, M., Lafeber, F.H., Lloyd, T., Aktas, B., Atlar, M., Turkmen, S., Seol, H., Hallander, J., Sakamoto, N., 2020. Noise measurements of a cavitating propeller in different facilities: results of the round robin test programme. Ocean. Eng. 213, 107599 https://doi.org/10.1016/j.oceaneng.2020.107599.
Testa, C., Porcacchia, F., Zaghi, S., Gennaretti, M., 2021. Study of a FWH-based permeable-surface formulation for propeller hydroacoustics. Ocean. Eng. 240, 109828 https://doi.org/10.1016/J.OCEANENG.2021.109828.
Testa, C., Procacchia, F., Greco, L., Muscari, R., 2018. Effectiveness of boundary element method hydrodynamic data for propeller hydroacoustics. In: A. Yucel Odabasi Colloquium Series 3rd International Meeting-Progress in Propeller Cavitation and its Consequences. Istanbul, Turkey.
Wang, M., B.Freund, J., K.Lele, S., 2018. Computational prediction of flow-generated sound. Annu. Rev. Fluid Mech. 50, 77–103. https://doi.org/10.1146/annurev.fluid.
Wang, M., Lele, S.K., Moin, P., 1996. Computation of quadrupole noise using acoustic analogy. AIAA J. 34, 2247–2254. https://doi.org/10.2514/3.13387.